Scale-discretised ridgelet transform on the sphere

Jason D. McEwen and Matthew A. Price

***Abstract*—We revisit the spherical Radon transform, also called the Funk-Radon transform, viewing it as an axisymmetric convolution on the sphere. Viewing the spherical Radon transform in this manner leads to a straightforward derivation of its spherical harmonic representation, from which we show the spherical Radon transform can be inverted exactly for signals exhibiting antipodal symmetry. We then construct a spherical ridgelet transform by composing the spherical Radon and scale-discretised wavelet transforms on the sphere. The resulting spherical ridgelet transform also admits exact inversion for antipodal signals. The restriction to antipodal signals is expected since the spherical Radon and ridgelet transforms themselves result in signals that exhibit antipodal symmetry. Our ridgelet transform is defined natively on the sphere, probes signal content globally along great circles, does not exhibit blocking artefacts, supports spin signals and exhibits an exact and explicit inverse transform. No alternative ridgelet construction on the sphere satisfies all of these properties. Our implementation of the spherical Radon and ridgelet transforms is made publicly available. Finally, we illustrate the effectiveness of spherical ridgelets for diffusion magnetic resonance imaging of white matter fibers in the brain.**

***Index Terms*—Harmonic analysis, spheres, spherical Radon transform, Funk Radon transform, spherical wavelets, spherical ridgelets.**

I. Introduction

WAVELET transforms on the sphere are becoming a standard tool for the analysis of data acquired on a spherical domain [1]–[26]. Of particular note are discrete wavelet frameworks on the sphere, which can support the exact synthesis of signals from their wavelet coefficients in a stable manner [6]–[11], [14]. Many of these frameworks have been extended to spin signal and signals on the three-ball [27]–[30].

However, the effectiveness of wavelets on the sphere is limited for highly anisotropic signal content. Directional scale-discretised wavelets on the sphere [9]–[11], [31], [32] go some way to addressing this shortcoming, however geometric properties of structures are not exploited. In Euclidean space, alternative transforms such as ridgelets and curvelets have been devised for such a purpose [33]–[36], which in turn (may) rely on the Radon transform [37], [38].

The spherical Radon transform, also called the Funk-Radon transform, is constructed from the integration of a signal along great circles [39]. In this letter we present a novel take on the spherical Radon transform, viewing it as a convolution with a kernel defined by a Dirac delta function in colatitude, such that it is non-zero along the equatorial great circle only. Viewing the spherical Radon transform in this manner helps to aid intuition, which leads to a straightforward derivation of its harmonic action (presented previously [40]–[42] in an alternative manner). In addition, we show that inversion of the spherical Radon transform is well-posed for signals that exhibit antipodal symmetry, *e.g.* in MRI analysis. While techniques that attempt to invert the spherical Radon transform are typically approximate [43]–[46], our inversion is exact and explicit.

First-generation ridgelets and curvelets were constructed on the sphere in [14]. However these wavelets are constructed by performing ridgelet and curvelet transforms of the twelve base-resolution faces of the HEALPIX pixelisation of the sphere [47] and so do not live natively on the sphere, do not probe signal content along great circles, and may result in blocking artefacts, as ackowledged in [14]. Second-generation curvelets have recently been developed [48] which live natively on the sphere, exhibit the parabolic scaling typical of curvelets, and do not suffer from blocking artefacts.

An alternative ridgelet transform on the sphere has been constructed in [49]. This construction lives natively on the sphere, probes signal content along great circles and does not exhibit any blocking artefacts. The ridgelet transform is constructed from a standard spherical Radon transform, followed by a wavelet transform on the sphere. Although this construction has already been demonstrated to be of considerable practical use [49], [50], the forward ridgelet transform is approximated in an iterative manner by an orthogonal matching pursuit algorithm and an explicit inversion is not given [49].

In this letter we develop a second-generation ridgelet transform on the sphere that exhibits all of the desirable properties of the construction of [49] and exhibits an explicit forward and inverse transform that can be computed efficiently and exactly for signals exhibiting antipodal symmetry. Moreover, our construction supports spin signals.

The letter is structured as follows. First, we present a novel take on the spherical Radon transform in Sec. II, viewing it as a convolution on the sphere, which leads to a straightforward derivation of its harmonic action. The spherical ridgelet transform is presented in Sec. III. The numerical implementation of our ridgelet transform is presented and evaluated in Sec. IV and an illustrative application to diffusion MRI is presented in Sec. V. Concluding remarks are made in Sec. VI.

II. Spherical Radon Transform

We present a novel take on the well-known spherical Radon transform, viewing it as an axisymmetric convolution, which leads to a straightforward derivation of its harmonic action.

This work was supported by the Engineering and Physical Sciences Research Council (grant number EP/M011852/1)

The authors are with the Mullard Space Science Laboratory (MSSL), University College London (UCL), Surrey RH5 6NT, UK.

E-mail: jason.mcewen@ucl.ac.uk

A. Axisymmetric convolution

The axisymmetric convolution $\odot$ of a function ${}_sf \in \mathrm{L}^2(\mathbb{S}^2)$ with an axisymmetric kernel ${}_sh \in \mathrm{L}^2(\mathbb{S}^2)$ is defined by

$$({}_sf \odot {}_sh)(\theta,\varphi) \equiv \langle {}_sf,\, \mathcal{R}_{(\theta,\varphi)}\,{}_sh\rangle = \int_{\mathbb{S}^2} \mathrm{d}\Omega(\theta',\varphi')\, f(\theta',\varphi')\, \big(\mathcal{R}_{(\theta,\varphi)}\,{}_sh\big)^*(\theta',\varphi')\,, \quad (1)$$

where we adopt the shorthand notation for the axisymmetric spherical rotation operator $\mathcal{R}_{(\beta,\alpha)} \equiv \mathcal{R}_{(\alpha,\beta,0)} \in \mathrm{SO}(3)$ parameterised by the Euler angles (α,β,γ). Axisymmetric convolution may be expressed by its harmonic expansion:

$$({}_sf \odot {}_sh)(\theta,\varphi) = \sum_{\ell=0}^{\infty} \sum_{m=-\ell}^{\ell} \sqrt{\frac{4\pi}{2\ell+1}}\, {}_sf_{\ell m}\, {}_sh^*_{\ell 0}\, Y_{\ell m}(\theta,\varphi)\,, \quad (2)$$

for spin harmonic coefficients ${}_sf_{\ell m} = \langle {}_sf,\, {}_sY_{\ell m}\rangle$ and ${}_sh_{\ell 0}\delta_{m0} = \langle {}_sh,\, {}_sY_{\ell m}\rangle$. Notice that although two spin functions are convolved, the resultant $({}_sf \odot {}_sh)$ is a scalar $(s=0)$ function on the sphere [31], [32].

B. Forward transform

The spherical Radon transform, also known as the Funk-Radon transform, is given by [39]

$$(\mathcal{S}_sf)(\theta,\varphi) \equiv \int_{\mathbb{S}^2} \mathrm{d}\Omega(\theta',\varphi')\, {}_sf(\theta',\varphi')\, \delta(\hat{\boldsymbol{\omega}}' \cdot \hat{\boldsymbol{\omega}})\,, \quad (3)$$

where $\hat{\boldsymbol{\omega}}$ and $\hat{\boldsymbol{\omega}}'$ denote the Cartesian vector corresponding to angular coordinates $\omega = (\theta,\varphi)$ and $\omega' = (\theta',\varphi')$, respectively. In words, the spherical Radon transform is the collection of line integrals of ${}_sf$ along great circles with poles at $\omega = (\theta,\varphi)$, projected onto the point defined by the poles of the great circles.

By defining the Funk-Radon kernel $\xi(\theta,\varphi) \equiv \delta(\theta - \pi/2)$, the spherical Radon transform $(\mathcal{S}_sf)(\theta,\varphi)$ may be expressed as an axisymmetric convolution by

$$({}_sf \odot \xi)(\theta,\varphi) = \int_{\mathbb{S}^2} \mathrm{d}\Omega(\theta',\varphi')\, {}_sf(\theta',\varphi')\, (\mathcal{R}_{(\theta,\varphi)}\xi)(\theta',\varphi').$$

Consequently, by noting Eq. (2), the spherical Radon transform can be expressed in harmonic space by

$$(\mathcal{S}_sf)_{\ell m} = ({}_sf \odot \xi)_{\ell m} = \sqrt{\frac{4\pi}{2\ell+1}}\, {}_sf_{\ell m}\, {}_s\xi^*_{\ell 0}\,, \quad (4)$$

where the harmonic coefficients of the Funk-Radon kernel read

$${}_s\xi_{\ell m} = (-1)^s \sqrt{\pi(2\ell+1)}\, \sqrt{\frac{(\ell-s)!}{(\ell+s)!}}\, P^s_\ell(0)\, \delta_{m0}\,. \quad (5)$$

Viewing the Funk-Radon transform as an axisymmetric convolution allows us to derive its harmonic representation in a straightforward manner as

$$(\mathcal{S}_sf)_{\ell m} = 2\pi\, (-1)^s \sqrt{\frac{(\ell-s)!}{(\ell+s)!}}\, P^s_\ell(0)\, {}_sf_{\ell m}\,. \quad (6)$$

C. Inverse transform

An inverse function to Eq. (6) exists if the associated Legendre functions are well-behaved at the origin. It can be shown that $P^s_\ell(0) = \mathcal{O}(\ell^{-1/2})$ as $\ell \to \infty$, for $s \ll \ell$ (which is typically the case in practice) and for $\ell + s$ even, while for $\ell + s$ odd, $P^s_\ell(0) = 0$. Concequently, the spherical Radon transform of signals with non-zero harmonic coefficients for $\ell + s$ even only, can be inverted by

$${}_sf_{\ell m} = (\mathcal{S}^{-1}\mathcal{S}_sf)_{\ell m} \equiv \frac{(\mathcal{S}_sf)_{\ell m}}{2\pi\, (-1)^s \sqrt{\frac{(\ell-s)!}{(\ell+s)!}}\, P^s_\ell(0)}\,. \quad (7)$$

For scalar signals, the restriction to signals with harmonic coefficients non-zero for even ℓ only corresponds to signals with antipodal symmetry – unsurpisingly, as the forward spherical Radon transform necessarily produces antipodal signals. In practice, inversion can be performed accurately up to very high ℓ.

D. Properties

We conclude our discussion of the spherical Radon transform by noting two important properties.

1) Shift invariance: The spherical Radon transform is shift invariant, such that

$$\big(\mathcal{S}\, \mathcal{R}_{(\alpha,\beta,\gamma)}\, {}_sf\big)(\theta,\varphi) = \big(\mathcal{R}_{(\alpha,\beta,\gamma)}\, \mathcal{S}\, {}_sf\big)(\theta,\varphi)\,. \quad (8)$$

2) Eigenfunctions and eigenvalues: By considering the spherical Radon transform of the spin spherical harmonics ${}_sY_{\ell m}$, we see from Eq. (6) that

$$(\mathcal{S}_s Y_{\ell m})(\theta,\varphi) = {}_s\lambda_\ell\, {}_sY_{\ell m}(\theta,\varphi)\,, \quad (9)$$

The spin spherical harmonics are therefore the eigenfunctions of the spherical Radon transform, with corresponding eigenvalues ${}_s\lambda_\ell = 2\pi\, (-1)^s \sqrt{\frac{(\ell-s)!}{(\ell+s)!}}\, P^s_\ell(0)$.

III. Spherical Ridgelet Transform

We present a novel spherical ridgelet transform on the sphere by composing the spherical Radon transform and the scale-discretised wavelet transform. Our construction permits an explicit inverse transform to synthesise antipodal signals from their ridgelet coefficients exactly and satisfies a number of additional desirable properties. For a complete review of scale-discretized wavelets see [9]–[11], [31], [32].

A. Ridgelet analysis and synthesis

We define the ridgelet transform on the sphere by the axisymmetric convolution with the ridgelet ${}_s\psi^{(j)} \in \mathrm{L}^2(\mathbb{S}^2)$:

$$G^{{}_s\psi^{(j)}}(\theta,\varphi) \equiv (\mathcal{G}^{{}_s\psi^{(j)}}\, {}_sf)(\theta,\varphi) \equiv ({}_sf \odot {}_s\psi^{(j)})(\theta,\varphi) = \int_{\mathbb{S}^2} \mathrm{d}\Omega(\theta',\varphi')\, {}_sf(\theta',\varphi')\, (\mathcal{R}_{(\theta,\varphi)}\, {}_s\psi^{(j)})(\theta',\varphi')\,, \quad (10)$$

with ridgelet coefficients $G^{{}_s\psi^{(j)}} \in \mathrm{L}^2(\mathbb{S}^2)$ defined on the sphere.

The rotated ridgelet $\mathcal{R}_{(\theta,\varphi)}\, {}_s\psi^{(j)}(\theta',\varphi')$ should be constant along the great circle defined by $\hat{\boldsymbol{\omega}} \cdot \hat{\boldsymbol{\omega}}' = 0$ and a wavelet transverse to the ridge defined by the great circle.

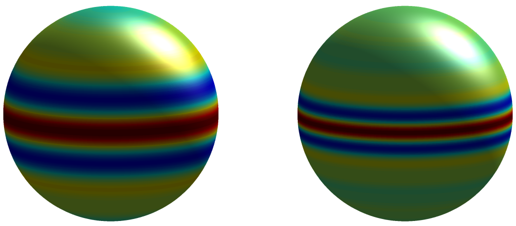

(a) Colour plot for $j = 3$ (b) Colour plot for $j = 4$

Fig. 1. Spherical ridgelets, with axis aligned with the North pole, for various wavelet scales. Notice that the constructed ridgelets are constant along ridges defined by great circles and wavelets transverse to ridges.

Such a ridgelet on the sphere can be constructed from an axisymmetric convolution of the Funk-Radon kernel ξ with the axisymmetric wavelet ${}_0\Psi^{(j)}$:

$$ {}_s\psi^{(j)}(\theta,\varphi) \equiv (\xi \odot {}_0\Psi^{(j)})(\theta,\varphi) \,. \tag{11} $$

In Fig. 1 ridgelets are plotted for various scales j. Notice that the ridgelets exhibit precisely the structure desired – probing signal content along great circles (*cf.* global lines).

The ridgelet transform of Eq. (10) can then be viewed as the composition of a spherical Radon transform followed by a wavelet transform:

$$ \begin{aligned} G^{{}_s\psi^{(j)}}(\theta,\varphi) &\equiv (\mathcal{G}^{{}_s\psi^{(j)}}\,{}_s f)(\theta,\varphi) \equiv ({}_s f \odot {}_s\psi^{(j)})(\theta,\varphi) \\ &= ({}_s f \odot \xi \odot {}_0\Psi^{(j)})(\theta,\varphi) \,. \end{aligned} \tag{12} $$

A ridgelet scaling function ${}_s\phi^{(j)} \in \mathrm{L}^2(\mathbb{S}^2)$ must be defined to capture the low-frequency content of the signal analysed:

$$ {}_s\phi^{(j)}(\theta,\varphi) \equiv (\xi \odot {}_0\Phi^{(j)})(\theta,\varphi) \,. \tag{13} $$

In terms of operators these relations can be written as,

$$ \mathcal{G}^{{}_s\psi^{(j)}} = \mathcal{W}^{{}_0\Psi^{(j)}}\mathcal{S} \quad \text{and} \quad \mathcal{G}^{{}_s\phi^{(j)}} = \mathcal{W}^{{}_0\Phi^{(j)}}\mathcal{S} \,. \tag{14} $$

We write the ridgelet transform for all ridgelets and the ridgelet scaling function by

$$ \boldsymbol{G}(\theta,\varphi) \equiv (\boldsymbol{\mathcal{G}}\,{}_s f)(\theta,\varphi) = ({}_0\boldsymbol{\mathcal{W}}\,\boldsymbol{\mathcal{S}}\,{}_s f)(\theta,\varphi) \,, \tag{15} $$

where bold notation represents a collection of coefficients.

For antipodal signals ${}_s f$ can be synthesised exactly from its ridgelet coefficients simply by:

$$ {}_s f(\theta,\varphi) = (\boldsymbol{\mathcal{S}}^{-1}\,{}_0\boldsymbol{\mathcal{W}}^{-1}\boldsymbol{G})(\theta,\varphi) \,. \tag{16} $$

IV. Evaluation

Our spherical Radon and ridgelet transforms have been added to the existing S2LET [10], [31] code that supports the exact and efficient computation of scale-discretised wavelet transforms on the sphere, which is publicly available[1], and relies on the SSHT[2] code [51] to compute spherical harmonic transforms and the FFTW[3] code to compute Fourier transforms. In this section we evaluate, on simulations of random antipodal signals on the sphere, the numerical accuracy, computation time and asymptotic scaling of the S2LET implementation of the ridgelet transform on the sphere.

[1] http://www.s2let.org
[2] http://www.spinsht.org
[3] http://www.fftw.org

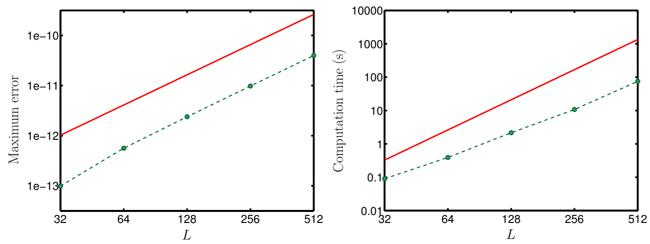

(a) Maximum error (b) Computation time

Fig. 2. Numerical accuracy and computation time of the spherical ridgelet transform, averaged over ten round-trip transforms of random test signals. Numerical accuracy close to machine precision is achieved and found empirically to scale as $\mathcal{O}(L^2)$, with a factor of $\mathcal{O}(L)$ coming from the inversion of each of the spherical Radon and spherical wavelet transforms. Computation time is found empirically to scale as $\mathcal{O}(L^3)$, as expected theoretically. $\mathcal{O}(L^2)$ and $\mathcal{O}(L^3)$ scaling is shown by the solid red lines in panels (a) and (b) respectively.

A. Simulations

We simulate band-limited test signals on the sphere defined by uniformly random spherical harmonic coefficients ${}_s f_{\ell m}$ with real and imaginary components in $[-1, 1]$. For $\ell + s$ odd we set harmonic coefficients to zero to satisfy the antipodal symmetry condition required for inversion. We then compute an inverse spherical harmonic transform to recover a band-limited signal on the sphere. A forward spherical ridgelet transform is then performed, followed by an inverse transform to synthesise the original signal from its ridgelet coefficients. Ten simulated signals are considered for range of band-limits L are considered (band-limits of at least $L = 4096$ are feasible; *cf.* [51]). All numerical experiments are performed on a 2011 Macbook Air, with a 1.8 GHz Intel Core i7 processor and 4 GB of RAM. Note that all numerical and computational results are identical when considering spin signals.

B. Numerical accuracy

Numerical accuracy is quantified by the maximum absolute error between the spherical harmonic coefficients of the original test signal ${}_s f^{\mathrm{o}}_{\ell m}$ and the recomputed values ${}_s f^{\mathrm{r}}_{\ell m}$, *i.e.* $\epsilon = \max_{\ell,m} \left| {}_s f^{\mathrm{r}}_{\ell m} - {}_s f^{\mathrm{o}}_{\ell m} \right|$. Results of the numerical accuracy tests, averaged over ten random test signals, are plotted in Fig. 2(a). The numerical accuracy of the round-trip transform is close to machine precision and found empirically to scale as $\mathcal{O}(L^2)$, with a factor of $\mathcal{O}(L)$ coming from both the inverse Radon and wavelet transforms.

C. Computation time

Computation time is quantified by the time taken to perform a forward and inverse spherical ridgelet transform. Results of the computation time tests, averaged over ten random test signals, are plotted in Fig. 2(b). The computational complexity of the ridgelet transform is dominated by the spherical harmonic transform, which scales as $\mathcal{O}(L^3)$, as seen in Fig. 2(b).

V. Illustration

In this section we illustrate the application of the spherical ridgelet transform to the analysis of diffusion MRI signals acquired on the sphere.

A. Diffusion MRI signals on the sphere

Diffusion MRI can be used to study neuronal connections by measuring the diffusion of water molecules along white matter fibers. In so-called high angular resolution diffusion imaging (HARDI), diffusion MRI signals are sampled on spherical shells in each voxel of the brain. The orientation distribution function (ODF) is approximately given by the spherical Radon transform of the HARDI signal acquired over a single spherical shell [52]. Often acquired data is noisy and incomplete, motivating the development of reqularized ODF recovery techniques (for a review see [53]).

The HARDI signal is modelled by a sum of weighted Gaussians, where each Gaussian corresponds to a different fiber passing through the voxel, and is given by (*e.g.* [49])

$$S(\hat{\boldsymbol{\omega}}) = \sum_i p_i \exp(-b\hat{\boldsymbol{\omega}}^{\mathrm{T}} \mathsf{D}_i \hat{\boldsymbol{\omega}}) , \tag{17}$$

where D_i is the 3×3 diffusion tensor corresponding to fiber i, b is an acquisition configuration constant, and p_i are fiber weights. We adopt the same parameters as the in silico experiments of [49]. Three fibers are considered, with D_i computed from D by random rotations. The simulated HARDI signal and the corresponding ODF are plotted in Fig. 3.

B. Diffusion MRI spherical ridgelet decomposition

Since the diffusion MRI HARDI signal is composed of a sum of contributions for each fibre that have their energy concentrated along great circles, it is suggested in [49], [50] that spherical ridgelets, which have their energy similarly distributed, are effective for representing HARDI signals and, in particular, more suitable than spherical wavelets. We demonstrate and validate these predictions by examining a HARDI signal in both spherical wavelet and ridgelet representations.

In Fig. 3 we plot wavelet and ridgelet coefficients of the HARDI signal simulated in Sec. V-A for a range of scales j. It is clear that ridgelet coefficients of the HARDI signal are sparser than wavelet coefficients, which exhibit many large peaks. For the ridgelet decompositions (Fig. 3, right column), the dominant directions of the ODF signal (Fig. 3(b)) are visible by eye, which is not the case for the wavelet decompositions (Fig. 3, left column). In Fig. 4 we plot histograms of wavelet and ridgelet coefficients for scale $j = 4$. The sparseness of HARDI signals in the spherical ridgelet decomposition, as demonstrated in this simple illustration, can be exploited in practical applications to handle noisy and incomplete data.

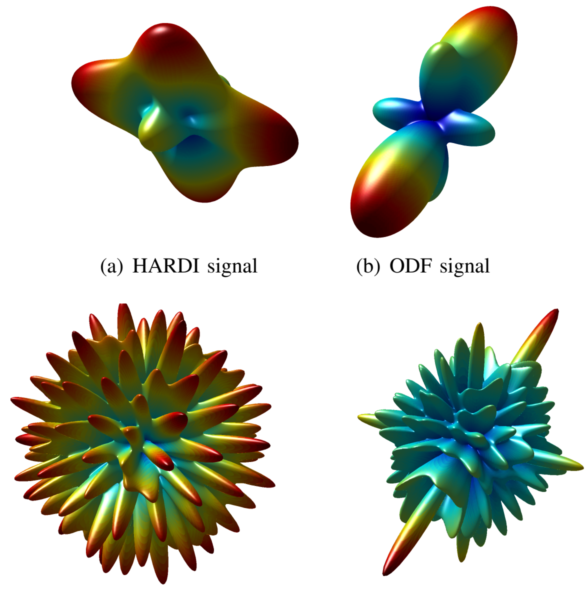

(a) HARDI signal (b) ODF signal

(c) Wavelet coefficients for $j = 5$ (d) Ridgelet coefficients for $j = 5$

Fig. 3. Parametric plots of spherical wavelet (left column, bottom) and ridgelet (right column, bottom) coefficients of the HARDI signal plotted in the top row. Notice that ridgelet coefficients are more sparse (*i.e.* fewer large coefficients) than the wavelet coefficients.

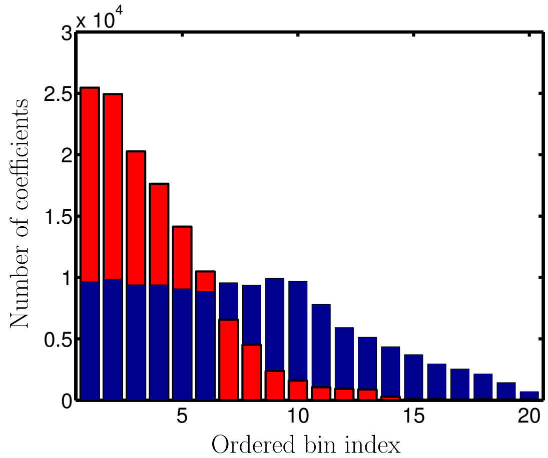

Fig. 4. Histogram of (the absolute value of) wavelet (blue) and ridgelet (red) coefficients for scale $j = 4$ of the HARDI signal plotted in Fig. 3(a). Notice that ridgelet coefficients are sparser than wavelet coefficients, with the ridgelet coefficients containing many coefficients close to zero and fewer large coefficients. The sparseness of the ridgelet coefficients of the HARDI signal demonstrates the suitability of spherical ridgelets for diffusion MRI.

VI. Conclusions

The publicly available ridgelet transform presented in this letter is defined natively on the sphere, probes signal content globally along great circles, does not exhibit blocking artefacts, supports spin signals, and exhibits an explicit inverse transform.

We present a novel take on the spherical Radon transform, viewing it as a convolution with an axisymmetric kernel. Such a representation leads to a straightforward derivation of the harmonic action of the spherical Radon transform, which motives an exact inversion technique for signals that exhibit antipodal symmetry. Consequently, our spherical ridgelet transform also permits the exact inversion for antipodal signals.

We demonstrate that the numerical accuracy of our transforms is close to machine precision and can be applied to large data-sets supporting high band-limits L, with computational complexity scaling as $\mathcal{O}(L^3)$. Finally, we illustrate the effectiveness of spherical ridgelets for imaging white matter fibers in the brain by diffusion MRI.

REFERENCES

[1] J.-P. Antoine and P. Vandergheynst, "Wavelets on the 2-sphere: a group theoretical approach," *ACHA*, vol. 7, pp. 1–30, 1999.

[2] ——, "Wavelets on the n-sphere and related manifolds," *J. Math. Phys.*, vol. 39, no. 8, pp. 3987–4008, 1998.

[3] Y. Wiaux, L. Jacques, and P. Vandergheynst, "Correspondence principle between spherical and Euclidean wavelets," *ApJ*, vol. 632, pp. 15–28, 2005.

[4] J. D. McEwen and A. M. M. Scaife, "Simulating full-sky interferometric observations," *MNRAS*, vol. 389, no. 3, pp. 1163–1178, 2008.

[5] J. D. McEwen, Y. Wiaux, and D. M. Eyers, "Data compression on the sphere," *A&A*, vol. 531, p. A98, 2011.

[6] F. J. Narcowich, P. Petrushev, and J. D. Ward, "Localized tight frames on spheres," *SIAM J. Math. Anal.*, vol. 38, no. 2, pp. 574–594, 2006.

[7] P. Baldi, G. Kerkyacharian, D. Marinucci, and D. Picard, "Asymptotics for spherical needlets," *Ann. Stat.*, vol. 37 No.3, pp. 1150–1171, 2009.

[8] D. Marinucci, D. Pietrobon, A. Balbi, P. Baldi, P. Cabella, G. Kerkyacharian, P. Natoli, D. Picard, and N. Vittorio, "Spherical needlets for cosmic microwave background data analysis," *MNRAS*, vol. 383, pp. 539–545, 2008.

[9] Y. Wiaux, J. D. McEwen, P. Vandergheynst, and O. Blanc, "Exact reconstruction with directional wavelets on the sphere," *MNRAS*, vol. 388, no. 2, pp. 770–788, 2008.

[10] B. Leistedt, J. D. McEwen, P. Vandergheynst, and Y. Wiaux, "S2LET: A code to perform fast wavelet analysis on the sphere," *A&A*, vol. 558, no. A128, pp. 1–9, 2013.

[11] J. D. McEwen, P. Vandergheynst, and Y. Wiaux, "On the computation of directional scale-discretized wavelet transforms on the sphere," in *SPIE Wavelets and Sparsity XV, invited contribution*, vol. 8858, 2013.

[12] J. L. Sanz, D. Herranz, M. López-Caniego, and F. Argüeso, "Wavelets on the sphere – application to the detection problem," in *EUSIPCO*, Sept. 2006.

[13] J. D. McEwen, M. P. Hobson, and A. N. Lasenby, "A directional continuous wavelet transform on the sphere," *ArXiv*, 2006.

[14] J.-L. Starck, Y. Moudden, P. Abrial, and M. Nguyen, "Wavelets, ridgelets and curvelets on the sphere," *A&A*, vol. 446, pp. 1191–1204, Feb. 2006.

[15] F. J. Simons, I. Loris, G. Nolet, I. C. Daubechies, S. Voronin, J. S. Judd, P. A. Vetter, J. Charléty, and C. Vonesch, "Solving or resolving global tomographic models with spherical wavelets, and the scale and sparsity of seismic heterogeneity," *GJI*, vol. 187, pp. 969–988, Nov. 2011.

[16] F. J. Simons, I. Loris, E. Brevdo, and I. C. Daubechies, "Wavelets and wavelet-like transforms on the sphere and their application to geophysical data inversion," in *SPIE Wavelets and Sparsity XIV*, 2011.

[17] P. Vielva, E. Martínez-González, R. B. Barreiro, J. L. Sanz, and L. Cayón, "Detection of non-Gaussianity in the WMAP 1-year data using spherical wavelets," *ApJ*, vol. 609, pp. 22–34, 2004.

[18] J. D. McEwen, M. P. Hobson, A. N. Lasenby, and D. J. Mortlock, "A high-significance detection of non-Gaussianity in the WMAP 1-year data using directional spherical wavelets," *MNRAS*, vol. 359, pp. 1583–1596, 2005.

[19] ——, "A high-significance detection of non-Gaussianity in the WMAP 3-year data using directional spherical wavelets," *MNRAS*, vol. 371, pp. L50–L54, 2006.

[20] ——, "A high-significance detection of non-Gaussianity in the WMAP 5-year data using directional spherical wavelets," *MNRAS*, vol. 388, no. 2, pp. 659–662, 2008.

[21] ——, "Non-Gaussianity detections in the Bianchi VII_h corrected WMAP 1-year data made with directional spherical wavelets," *MNRAS*, vol. 369, pp. 1858–1868, 2006.

[22] J. D. McEwen, P. Vielva, M. P. Hobson, E. Martínez-González, and A. N. Lasenby, "Detection of the ISW effect and corresponding dark energy constraints made with directional spherical wavelets," *MNRAS*, vol. 373, pp. 1211–1226, 2007.

[23] J. D. McEwen, Y. Wiaux, M. P. Hobson, P. Vandergheynst, and A. N. Lasenby, "Probing dark energy with steerable wavelets through correlation of WMAP and NVSS local morphological measures," *MNRAS*, vol. 384, no. 4, pp. 1289–1300, 2008.

[24] Planck Collaboration XII, "*Planck 2013* results. XII. Diffuse component separation," *A&A*, vol. 571, p. A12, 2014.

[25] Planck Collaboration XXIII, "*Planck* 2013 results. XXIII. Isotropy and statistics of the CMB," *A&A*, vol. 571, no. A23, 2014.

[26] Planck Collaboration XXV, "*Planck* 2013 results. XXV. Searches for cosmic strings and other topological defects," *A&A*, vol. 571, no. A25, 2014.

[27] C. Durastanti, Y. Fantaye, F. Hansen, D. Marinucci, and I. Z. Pesenson, "Simple proposal for radial 3D needlets," *PRD*, vol. 90, no. 10, p. 103532, Nov. 2014.

[28] B. Leistedt and J. D. McEwen, "Exact wavelets on the ball," *IEEE TSP*, vol. 60, no. 12, pp. 6257–6269, 2012.

[29] J. D. McEwen and B. Leistedt, "Fourier-Laguerre transform, convolution and wavelets on the ball," in *SampTA, invited contribution*, 2013, pp. 329–333.

[30] F. Lanusse, A. Rassat, and J.-L. Starck, "Spherical 3D isotropic wavelets," *A&A*, vol. 540, p. A92, Apr. 2012.

[31] J. D. McEwen, B. Leistedt, M. Büttner, and H. V. Peiris, "Directional spin wavelets on the sphere," *arXiv:1509.06749*, 2015.

[32] J. D. McEwen, C. Durastanti, and Y. Wiaux, "Localisation of directional scale-discretised wavelets on the sphere," *ACHA*, vol. 44, no. 1, pp. 59–88, 2018.

[33] E. J. Candès and D. L. Donoho, "Ridgelets: a key to higher-dimensional intermittency?" *Philosophical Transactions of the Royal Society of London A: Mathematical, Physical and Engineering Sciences*, vol. 357, no. 1760, pp. 2495–2509, 1999.

[34] E. Candès and D. Donoho, "Curvelets: A Surprisingly Effective Nonadaptive Representation of Objects with Edges," L. L. S. et al., Ed. Nashville, TN: Vanderbilt University Press, 1999.

[35] ——, "Continuous curvelet transform: I. resolution of the wavefront set," *ACHA*, vol. 19, no. 2, pp. 162–197, 2005.

[36] ——, "Continuous curvelet transform: Ii. discretization and frames," *ACHA*, vol. 19, no. 2, pp. 198–222, 2005.

[37] J. Radon, "Uber die bestimmung von funktionen durch ihre integralwerte lngs gewisser mannigfaltigkeiten," *Royal Saxonian Academy of Sciences*, vol. 69, pp. 262–277, 1917.

[38] ——, "On the determination of functions from their integral values along certain manifolds," *Medical Imaging, IEEE Transactions on*, vol. 5, no. 4, pp. 170–176, Dec 1986.

[39] P. Funk, "Uber eine geometrische anwendung der abelschen integralgleichung," *Math. Ann.*, vol. 77, pp. 129–135, 1916.

[40] A. W. Anderson, "Measurement of fiber orientation distributions using high angular resolution diffusion imaging," *Magnetic Resonance in Medicine*, vol. 54, no. 5, pp. 1194–1206, 2005.

[41] M. Descoteaux, E. Angelino, S. Fitzgibbons, and R. Deriche, "Regularized, fast, and robust analytical q-ball imaging," *Magnetic Resonance in Medicine*, vol. 58, no. 3, pp. 497–510, 2007.

[42] C. P. Hess, P. Mukherjee, E. T. Han, D. Xu, and D. B. Vigneron, "Q-ball reconstruction of multimodal fiber orientations using the spherical harmonic basis," *Magnetic Resonance in Medicine*, vol. 56, no. 1, pp. 104–117, 2006.

[43] L.-E. Andersson, "On the determination of a function from spherical averages," *SIAM Journal on Mathematical Analysis*, vol. 19, no. 1, pp. 214–232, 1988.

[44] J. Klein, "Inverting the spherical Radon transform for physically meaningful functions," *ArXiv Mathematics e-prints*, July 2003.

[45] A. K. Louis, M. Riplinger, M. Spiess, and E. Spodarev, "Inversion algorithms for the spherical radon and cosine transform," *Inverse Problems*, vol. 27, no. 3, p. 035015, 2011.

[46] R. Regnier, G. Rigaud, and M. Nguyen, "New approximated inversion of spherical radon transform in sar imaging," in *Image Processing (ICIP), 2013 20th IEEE International Conference on*, Sept 2013, pp. 2398–2401.

[47] K. M. Górski, E. Hivon, A. J. Banday, B. D. Wandelt, F. K. Hansen, M. Reinecke, and M. Bartelmann, "Healpix – a framework for high resolution discretization and fast analysis of data distributed on the sphere," *ApJ*, vol. 622, pp. 759–771, 2005.

[48] J. Y. H. Chan, B. Leistedt, T. D. Kitching, and J. D. McEwen, "Second-generation curvelets on the sphere," *IEEE TSP*, vol. 65, no. 1, pp. 5–14, 2016.

[49] O. Michailovich and Y. Rathi, "On approximation of orientation distributions by means of spherical ridgelets," *IEEE TIP*, vol. 19, no. 2, pp. 461–477, Feb 2010.

[50] ——, "Spatially regularized q-ball imaging using spherical ridgelets," in *Biomedical Imaging: From Nano to Macro, 2010 IEEE International Symposium on*, April 2010, pp. 1181–1184.

[51] J. D. McEwen and Y. Wiaux, "A novel sampling theorem on the sphere," *IEEE TSP*, vol. 59, no. 12, pp. 5876–5887, 2011.

[52] D. S. Tuch, "Q-ball imaging," *Magn. Reson. Med.*, vol. 52, no. 6, pp. 1358–1372, 2004.

[53] D. C. Alexander, "Multiple-fiber reconstruction algorithms for diffusion mri," *Annals of the New York Academy of Sciences*, vol. 1064, no. 1, pp. 113–133, 2005.